FERROELECTRICS

Stacking-engineered ferroelectricity in bilayer boron nitride

Kenji Yasuda[1]*, Xirui Wang[1], Kenji Watanabe[2], Takashi Taniguchi[2], Pablo Jarillo-Herrero[1]*
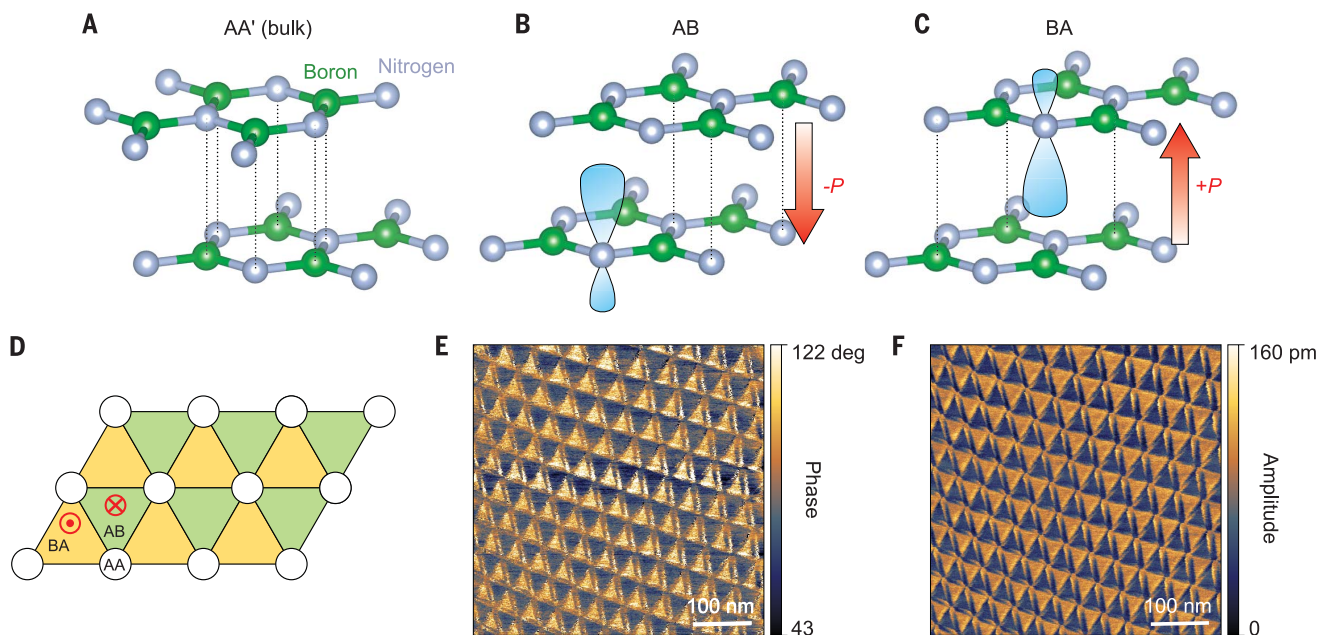
Two-dimensional (2D) ferroelectrics with robust polarization down to atomic thicknesses provide building blocks for functional heterostructures. Experimental realization remains challenging because of the requirement of a layered polar crystal. Here, we demonstrate a rational design approach to engineering 2D ferroelectrics from a nonferroelectric parent compound by using van der Waals assembly. Parallel-stacked bilayer boron nitride exhibits out-of-plane electric polarization that reverses depending on the stacking order. The polarization switching is probed through the resistance of an adjacently stacked graphene sheet. Twisting the boron nitride sheets by a small angle changes the dynamics of switching because of the formation of moiré ferroelectricity with staggered polarization. The ferroelectricity persists to room temperature while keeping the high mobility of graphene, paving the way for potential ultrathin nonvolatile memory applications.

F erroelectric materials with an electric-field switchable polarization offer a wide range of technological applications, such as nonvolatile memories, high-permittivity dielectrics, electromechanical actuators, and pyroelectric sensors (1). Thinning down vertical ferroelectrics is one of the essential steps for the implementation of ferroelectric nonvolatile memory as part of the quest for denser storage and lower power consumption (1). Room-temperature ferroelectricity down to atomic thicknesses was, however, difficult to access because of the depolarization effect until the recent development of three series of materials: epitaxial perovskites (2, 3), HfO_2-based ferroelectrics (4), and low-dimensional van der Waals (vdW) ferroelectrics (5–13). Among them, 2D vdW ferroelectrics present opportunities to integrate high-mobility materials such as graphene into ferroelectric field-effect transistors while keeping their properties intact, attributable to the absence of dangling bonds (14). Their uniform atomic thickness

also makes them ideal as ferroelectric tunnel barriers for use in ferroelectric tunnel junctions (15). Despite the potential importance for application as a ferroelectric memory, only a few examples of 2D vertical ferroelectrics— $CuInP_2S_6$, In_2Se_3, $MoTe_2$, and WTe_2—have been discovered so far (9–13); the candidate materials have been largely limited by the requirement of the polar space group in the original layered bulk crystal.

The development of vdW assembly enabled the engineering of heterostructures with physical properties beyond the sum of those of the individual layers (16). For example, the Dirac band structure of graphene is dramatically transformed when it is aligned with hexagonal boron nitride (hBN) or stacked with another slightly rotated graphene sheet. The modified band structures have led to the discovery of a variety of emergent phenomena related to electron correlations and topology beyond expectations from the original band structure (17–24). Here, we demonstrate that the vdW stacking modifies not only the electronic band structure but also the crystal symmetry, thereby enabling the design of ferroelectric materials out of nonferroelectric parent compounds. We use BN as an example, but the same procedure can be applied to other bipartite honeycomb 2D materials, such as 2H-type transition metal dichalcogenides (TMDs) (25). Bulk hBN crystals realize AA' stacking, as shown in Fig. 1A. This 180°-rotated natural stacking order restores

[1]Department of Physics, Massachusetts Institute of Technology, Cambridge, MA 02139, USA. [2]National Institute for Materials Science, Namiki 1-1, Tsukuba, Ibaraki 305-0044, Japan.
*Corresponding author. Email: yasuda@mit.edu (K.Y.); pjarillo@mit.edu (P.J.-H.)

Fig. 1. Polarization in AB-stacked bilayer BN. (**A**) Illustration of the atomic arrangement for AA' stacking, the bulk form of hBN. Nitrogen and boron atoms are shown in silver and green, respectively. (**B** and **C**) Illustration of the atomic arrangement for AB and BA stacking. The vertical alignment of nitrogen and boron atoms distorts the $2p_z$ orbital of nitrogen (light blue), creating an out-of-plane electric dipole. (**D**) Illustration of a small-angle twisted bilayer BN after the atomic reconstruction. The reconstruction creates relatively large AB (green) and BA (yellow) domains, with small AA regions (white) and domain walls in between (black). The red circled dot and red circled X represent up and down polarization, respectively. (**E** and **F**) Vertical PFM phase and amplitude images of twisted bilayer BN. Scale bars are 100 nm. The contrast at the domain wall, different from the AB and BA domain regions, likely originates from the flexoelectric effect (36, 42).
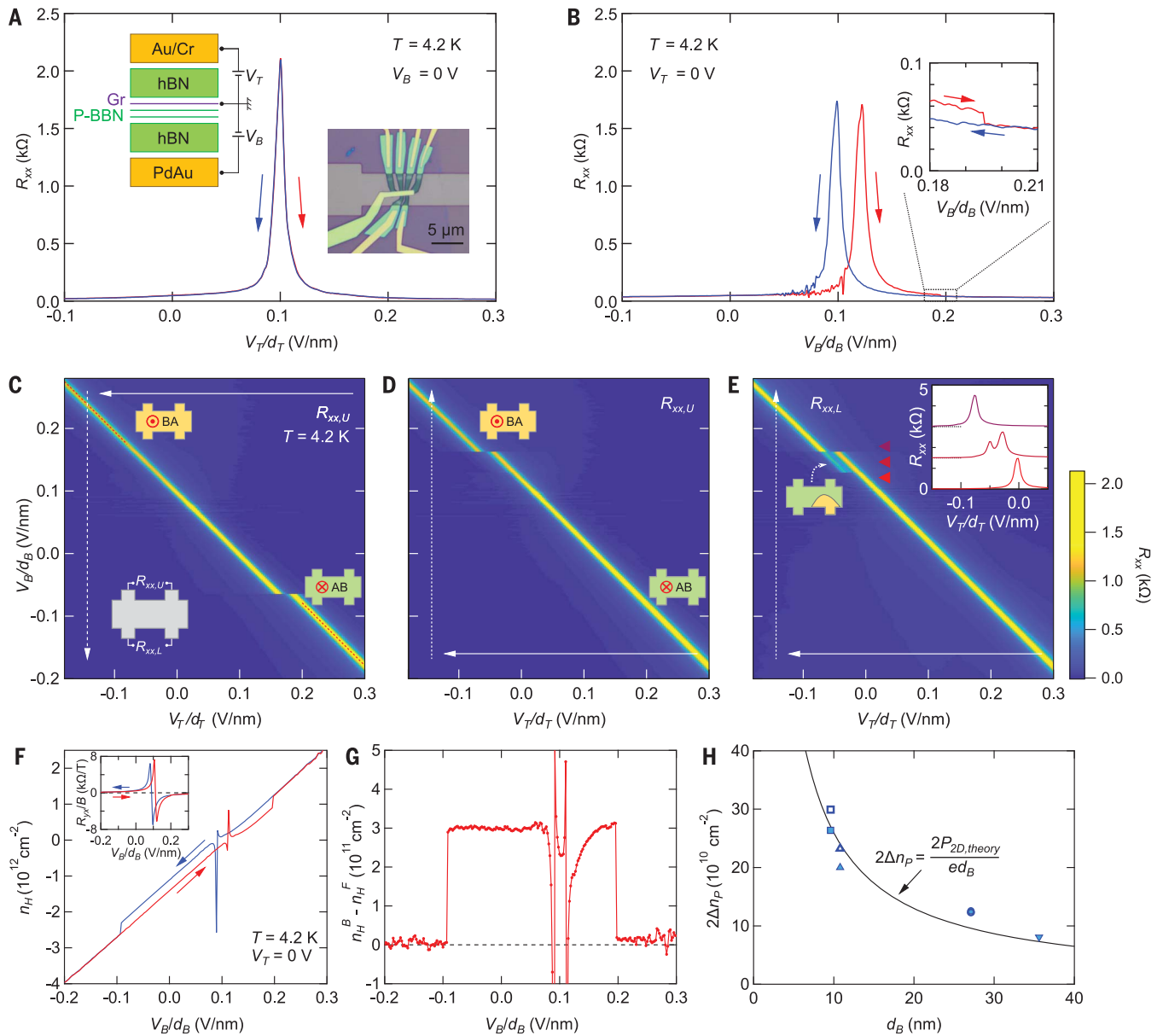
Fig. 2. Ferroelectric switching in parallel-stacked bilayer BN. (A) Resistance R_{xx} of graphene for device P1 as a function of V_T/d_T, the top gate voltage V_T divided by the thickness of top hBN d_T. V_T/d_T is scanned in the backward (forward) direction starting from +0.36 V/nm (−0.36 V/nm) in the blue (red) curve. Note that we only show the relevant scan range around the resistance peak in the figure. The inset on the left shows the schematic device structure. The inset on the right shows an optical micrograph of the device. Gr, graphene. **(B)** Resistance R_{xx} as a function of V_B/d_B, the bottom gate voltage V_B divided by the distance between graphene and bottom gate electrode d_B. V_B/d_B is scanned in the backward (forward) direction starting from +0.42 V/nm (−0.42 V/nm) in the blue (red) curve. The inset shows the enlarged plot around 0.20 V/nm. **(C)** Resistance $R_{xx,U}$ measured with the upper voltage contacts of device P1 (as displayed in the inset on the lower left) as a function of V_B/d_B and V_T/d_T. We repeatedly scanned V_T/d_T (fast scan, solid arrow) in the backward direction while gradually changing V_B/d_B (slow scan, dashed arrow). V_B/d_B is changed in the backward direction starting from +0.42 V/nm. Note that we only show the relevant scan range in the figure. The insets on the upper left and lower right show the schematic domain configuration and the polarization direction (red circled dot and red circled X).

The red dashed lines represent the charge neutrality points. **(D)** The same as (C) with V_B/d_B changed in the forward direction starting from −0.42 V/nm. **(E)** The same as (D) for the resistance $R_{xx,L}$ measured with the lower voltage contacts. The inset on the right shows the line cuts at the fixed V_B/d_B locations indicated by the red triangles. Each curve is offset by 1.5 kilohms for clarity. The inset on the left shows the schematic domain configuration during the ferroelectric switching (fig. S15). **(F)** Hall carrier density n_H measured as a function of V_B/d_B. V_B/d_B is scanned in the backward (forward) direction starting from +0.42 V/nm (−0.42 V/nm) in the blue (red) curve. The inset shows the Hall resistance R_{yx} as a function of V_B/d_B under magnetic field (B) = 0.5 T. **(G)** The difference of Hall carrier density in the backward and forward scan, $n_H^B - n_H^F$. **(H)** Twice the induced carrier density by the polarization of P-BBN, $2\Delta n_P$, plotted against d_B for four devices studied in this work. The $2\Delta n_P$ of each device is shown with a different shape; square (P1), triangle (P2), inverse-triangle (T1), and circle (T2). The filled and hollow symbols represent $2\Delta n_P$ estimated from the horizontal shift of the resistance peak and the Hall resistance, respectively. Note that two markers of device T2 almost overlap with each other. The black curve is the theoretical curve calculated from the polarization obtained from the Berry phase calculation, $P_{2D,theory}$ (25).

Fig. 3. Ferroelectric switching in twisted bilayer BN. (**A**) Resistance R_{xx} of device T1 as a function of V_B/d_B and V_T/d_T. The insets show schematic illustrations of the domain configurations. We repeatedly scanned V_T/d_T (fast scan, solid arrow) while gradually changing V_B/d_B (slow scan, dashed arrow). V_B/d_B is changed in the backward direction starting from +0.42 V/nm. The size of the domain is not to scale. (**B**) Spatial average of polarization of bilayer BN, $\langle P \rangle$, estimated from the two-peak fitting as a function of the applied electric field V_B/d_B for a twisted device, T1 (solid lines), and a nontwisted device, P1 (dashed lines). The blue and red curves are backward and forward scans, respectively. $\langle P \rangle$ of device P1 is estimated by taking the average of the polarization measured with the upper voltage contacts and the lower voltage contacts. We expect that small, but finite, AB (BA) regions remain, even at $\langle P \rangle = 1(-1)$, in a twisted device as depicted in the insets of (A), although they are too small to be clearly detected with our resistance measurement scheme.
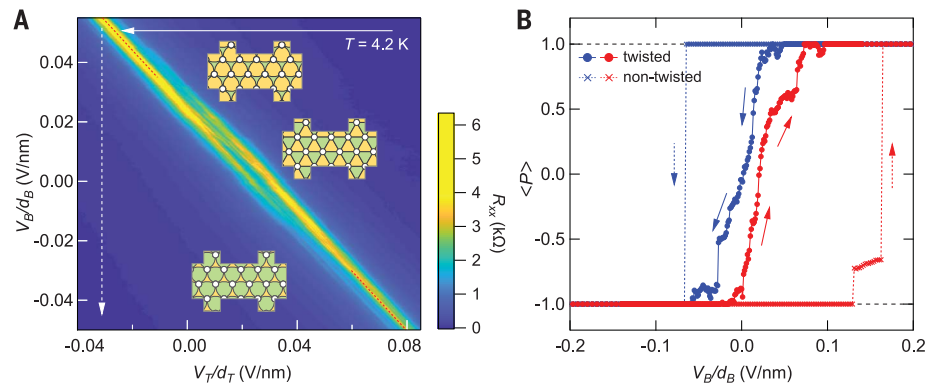
the inversion symmetry broken in the monolayer. However, if two BN monolayer sheets are stacked without rotation (parallel stacking, P), it has been theoretically (*26, 27*) and experimentally (*28–31*) shown that polar AB or BA stacking orders (Fig. 1, B and C, respectively) are formed. These configurations are local energy minima in a parallel-stacked form and are realized as metastable crystal structures (*26, 27*). In AB (BA) stacking, the B (N) atoms in the upper layer sit above the N (B) atoms in the lower layer while the N (B) atoms in the upper layer lay above the empty site at the center of the hexagon in the lower layer. The vertical alignment of the $2p_z$ orbitals of N and B distorts the orbital of N, creating an electric dipole moment (fig. S3). As a result, AB and BA stacking will exhibit out-of-plane polarization in the opposite directions (*25*).

We demonstrate the polarization of AB-stacked bilayer BN by vertical piezoelectric force microscopy (PFM). We fabricated nearly 0° bilayer BN devices by using the "tear and stack" method, where half of a monolayer BN flake is picked up and stacked on top of the remaining half (*32, 33*). In twisted bilayer BN, lattice relaxation leads to the formation of a moiré pattern consisting of AB and BA lattice networks with topological defects (AA regions), as in the case of twisted bilayer graphene and TMDs (Fig. 1D) (*34–36*). However, unlike twisted bilayer graphene, the low crystalline symmetry of BN creates a distinctive moiré pattern with staggered polarization in the AB and BA domains (*25*). PFM measurements on a small-angle twisted bilayer BN show a triangular pattern with finite contrast between the adjacent triangles (Fig. 1, E and F), whereas no moiré pattern is observed in the topographic image (fig. S6). The different piezoresponse in the AB and BA domains evidences the opposite out-of-plane polarizations in these domains. In a larger area scan (figs. S7 and S8), the periodicity of the triangular pattern varies at wrinkles and bubbles as the rotational angle changes. The triangular contrast

does not show up in the monolayer BN region, confirming the interlayer interaction origin of the polarization (figs. S7 and S8). The stacking order–dependent out-of-plane polarization presents the interesting possibility that the polarization can be switched by an in-plane interlayer shear motion of one-third of the unit cell (*25*), which is distinct from the switching mechanism of conventional ferroelectrics (*1*).

To study the change of the polarization under the electric field, we fabricated dual-gated vdW heterostructure devices composed of metal top gate (Au/Cr)/hBN/graphene/0° parallel stacked bilayer BN (P-BBN)/hBN/metal bottom gate (PdAu) (e.g., device P1), as schematically shown in the inset of Fig. 2A. Zero-degree stacking of P-BBN allows the entire region to be a single domain of AB or BA stacking without forming the moiré pattern. Here, the graphene sensitively detects the extra charge carriers induced by the polarization of P-BBN. Figure 2A shows the resistance of the graphene sensor as a function of the top gate voltage, V_T (for both forward and backward gate sweep directions), which exhibits a typical maximum without hysteresis. By contrast, the forward and backward scans of the resistance versus the bottom gate voltage, V_B (Fig. 2B) shows hysteresis, exhibiting maxima at about 0.10 and 0.12 V/nm for the backward and forward scans, respectively. In addition, we observe a resistance step at around 0.20 V/nm in the forward scan, as displayed in the inset. As discussed later, this bistability is attributed to the polarization switching of P-BBN by the applied electric field.

Dual-gate scanning allows independent control of the carrier density of graphene and the electric field across the P-BBN, because the top gate primarily changes the former (figs. S10 and S11), whereas the bottom gate changes both. In a standard dual-gated graphene device, a measurement of the resistance versus the top and bottom gate voltages results in a single diagonal feature, a maximum resistance ridge, corresponding to the charge neutrality condi-

tion. The diagonal feature stems from the fact that the induced carrier density follows the equation $n = \varepsilon_{hBN}(V_B/d_B + V_T/d_T)/e$, where ε_{hBN} is the dielectric constant of hBN, d_B (d_T) is the distance between graphene and the bottom (top) gate electrode, and e is the elemental charge. By contrast, two parallel-shifted diagonal lines are observed in a dual-gate scan for our P-BBN device (Fig. 2C). The shift reflects an abrupt change in the induced carrier density, Δn_P, caused by the switching of the electric polarization of P-BBN: As the polarization switches from up (BA stacking) to down (AB stacking) at $V_B/d_B = -0.06$ V/nm, the total induced carrier density changes from $\varepsilon_{hBN}(V_B/d_B + V_T/d_T)/e + \Delta n_P$ to $\varepsilon_{hBN}(V_B/d_B + V_T/d_T)/e - \Delta n_P$, leading to the shift of the charge neutrality resistance peak. Similarly, the forward scan of the bottom gate shows the polarization switching from down to up at $V_B/d_B = 0.16$ V/nm (Fig. 2D). Notably, the resistance measured using the lower voltage contacts exhibits an intermediate, two-peak behavior during the switching (Fig. 2E). This indicates the coexistence of micrometer-scale AB and BA domains and provides a hint to the dynamics of polarization switching. Namely, the domain wall is pinned in the middle of the Hall bar at around $V_B/d_B = 0.13$ V/nm, followed by the depinning at around $V_B/d_B = 0.16$ V/nm.

To further investigate the ferroelectric properties of P-BBN, we measured the carrier density n_H of graphene extracted from Hall resistance measurements (Fig. 2F). Hysteretic behavior with an abrupt jump in n_H is observed when sweeping V_B, which is attributed to the ferroelectric switching. The subtraction of the forward and backward sweeps gives a magnitude of $2\Delta n_P$, which equals 3.0×10^{11} cm^{-2} (Fig. 2G). This value is consistent with $2\Delta n_P = 2.6 \times 10^{11}$ cm^{-2} estimated from the horizontal shift of the charge neutrality resistance peak in the dual-gate scan (Fig. 2, C to E). Δn_P allows us to calculate the magnitude of the polarization of AB-stacked bilayer BN. According to a simple model calculation (see fig. S14 for details), the
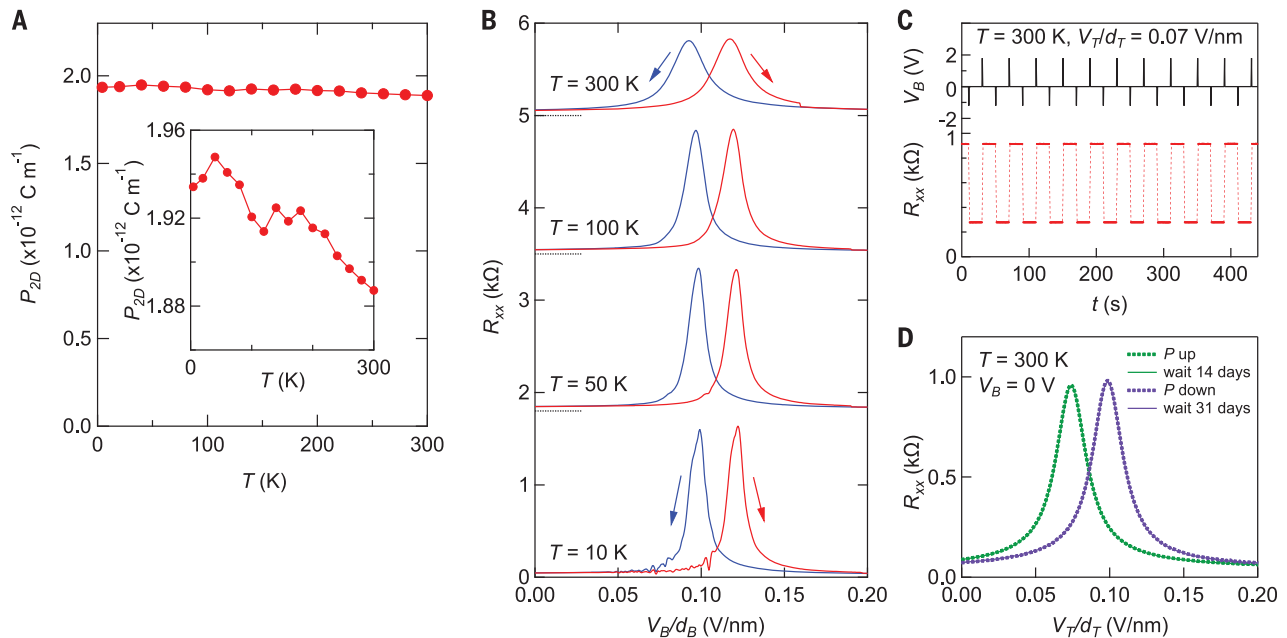
Fig. 4. Room-temperature operation of a ferroelectric field-effect transistor.
(**A**) Temperature dependence of the magnitude of the polarization P_{2D} for device P1. The inset shows a zoom-in of the vertical axis. (**B**) Hysteresis of resistance at various temperatures. V_B/d_B is scanned in the backward (forward) direction starting from +0.42 V/nm (−0.42 V/nm) in the blue (red) curve. Each curve is offset for clarity. The offset values are shown as dotted lines. (**C**) Resistance (red curve) after the repeated application of a voltage pulse of V_B = +1.8 V and V_B = −1.2 V (black curve), which corresponds to V_B/d_B = +0.19 and −0.13 V/nm, respectively. The measurement is performed at T = 300 K and V_T/d_T = 0.07 V/nm. (**D**) Stability of polarization at room temperature. V_T/d_T is scanned in the forward direction. The dotted green (purple) curve is measured at V_B = 0 V right after applying V_B/d_B = +0.31 V/nm (−0.26 V/nm) to induce polarization up (down). The solid green curve is measured after applying V_B/d_B = +0.31 V/nm to induce polarization up and then leaving the device at V_B = 0 V and T = 300 K for 14 days. The solid purple curve is measured after applying V_B/d_B = −0.26 V/nm to induce polarization down and then leaving the device at V_B = 0 V and T = 300 K for 31 days. Each of the two curves almost exactly overlap, showing the robustness of polarization direction for a long period.

2D polarization follows $P_{2D} = e\Delta n_P d_B$; namely, the electric dipole moment between the bottom gate and graphene is equal to the magnitude of the polarization of bilayer BN. Figure 2H shows our measurement of $2\Delta n_P$ for four different devices studied in this work, which indeed exhibit an inverse proportional behavior with respect to d_B. The magnitude of the polarization estimated from these data points is P_{2D} = 2.25 (0.37) × 10^{-12} C m^{-1} (corresponding to P_{3D} = 0.68 μC cm^{-2}). This agrees well with the theoretically calculated magnitude of the polarization of AB-stacked bilayer BN from a Berry phase calculation, $P_{2D,theory}$ = 2.08 × 10^{-12} C m^{-1} (25, 37).

Having established the ferroelectric nature of P-BBN, we next studied how the moiré superlattice affects the ferroelectric switching in a small-angle twisted bilayer BN. Here, owing to the opposite polarization of AB and BA stacking regions (Fig. 1, D to F), each domain with staggered polarization is expected to expand or shrink, through domain wall motion, when a vertical electric field is applied. Figure 3A shows the dual-gate scan of the resistance of graphene for a 0.6°–rotation angle twisted bilayer BN (device T1). It exhibits two parallel diagonal peaks, each corresponding to the AB or BA domains, similar to Fig. 2C. However, rather than an abrupt

transition between the two lines, a gradual shift in weight from one to the other takes place along the diagonal. Thus, the magnitude of each peak gives the relative proportion of AB and BA domain sizes, or the average polarization, as a function of the applied electric field (fig. S17). The electric field dependence of the polarization (Fig. 3B) highlights the difference between the twisted and nontwisted devices. First, the coercive field is much smaller for the twisted bilayer BN than for the nontwisted P-BBN. Secondly, the polarization switching occurs gradually, in contrast to the sharp switching of the nontwisted device. In a nontwisted device, a domain wall moves over the device scale during the switching, as shown in Fig. 2, C to E, and is likely to be pinned by strong pinning centers. By contrast, each domain wall in a twisted device moves only by a moiré length scale and will experience weaker pinning centers, leading to the small coercive field. In addition, the different pinning strength of each domain wall leads to the gradual switching. Thus, the global rotation of the two layers modifies the dynamics of the ferroelectric switching behavior.

Finally, we studied the temperature dependence of the ferroelectricity in P-BBN. Notably, the polarization measured from Δn_P is almost independent of temperature (Fig. 4A

and fig. S22) up to room temperature. The nearly temperature-independent ferroelectric polarization presumably reflects the distinctive coupling between the out-of-plane polarization and the in-plane shear motion in P-BBN. The strong intralayer covalent bonding inhibits the in-plane thermal vibration of atoms, making the polarization insensitive to temperature (38). Correspondingly, the ferroelectric hysteresis is observable up to room temperature despite the temperature-induced broadening of the resistance peak (Fig. 4B). Such hysteretic behavior allows us to deterministically write the polarization by a voltage pulse of only a few volts and read it in a nonvolatile way, as shown in Fig. 4C. We also checked the stability of the ferroelectric polarization by keeping the sample at 0 V at room temperature for an extended period after setting the polarization to up or down (Fig. 4D). The resistance remains almost the same after at least a month (the longest period measured); namely, P-BBN retains its polarization over a technologically relevant time scale. Hence, the present result points to the potential use of P-BBN/graphene as a ferroelectric field-effect transistor with an ultrahigh mobility of graphene of around 5 × 10^4 cm^2 V^{-1} s^{-1} at room temperature (figs. S19 to S21).

The designer approach for engineering vdW ferroelectrics and moiré ferroelectrics

4 of 5

demonstrated in this study can be extended to other bipartite honeycomb 2D materials, such as semiconducting 2H-type TMDs like MoS_2 and WSe_2, metallic and superconducting ones like NbS_2 and $NbSe_2$, and group III chalcogenides like GaS, GaSe, and InSe (25). The inversion symmetry breaking of these synthetic ferroelectrics will be coupled to the electronic band structures in a tunable manner through polarization switching. In addition to interesting physics resulting from the modification of the intrinsic properties of each material, such engineered ferroelectrics and moiré systems may substantially expand the capabilities of 2D materials for electronic, spintronic, and optical applications (15, 39).

We note that (40) and a paper in the same issue (41) report related findings.

REFERENCES AND NOTES

1. K. Uchino, *Ferroelectric Devices* (CRC Press, 2009).
2. D. D. Fong *et al.*, *Science* **304**, 1650–1653 (2004).
3. H. Wang *et al.*, *Nat. Commun.* **9**, 3319 (2018).
4. U. Schröeder, C. S. Hwang, H. Funakubo, *Ferroelectricity in Doped Hafnium Oxide: Materials, Properties and Devices* (Woodhead Publishing, 2019).
5. C. Cui, F. Xue, W.-J. Hu, L.-J. Li, *npj 2D Mater. Appl.* **2**, 18 (2018).
6. M. Wu, P. Jena, *Wiley Interdisc. Rev. Comput. Mol. Sci.* **8**, e1365 (2018).
7. A. V. Bune *et al.*, *Nature* **391**, 874–877 (1998).
8. K. Chang *et al.*, *Science* **353**, 274–278 (2016).
9. F. Liu *et al.*, *Nat. Commun.* **7**, 12357 (2016).
10. Y. Zhou *et al.*, *Nano Lett.* **17**, 5508–5513 (2017).
11. C. Cui *et al.*, *Nano Lett.* **18**, 1253–1258 (2018).
12. S. Yuan *et al.*, *Nat. Commun.* **10**, 1775 (2019).
13. Z. Fei *et al.*, *Nature* **560**, 336–339 (2018).
14. C. R. Dean *et al.*, *Nat. Nanotechnol.* **5**, 722–726 (2010).
15. E. Y. Tsymbal, H. Kohlstedt, *Science* **313**, 181–183 (2006).
16. A. K. Geim, I. V. Grigorieva, *Nature* **499**, 419–425 (2013).
17. B. Hunt *et al.*, *Science* **340**, 1427–1430 (2013).
18. C. R. Dean *et al.*, *Nature* **497**, 598–602 (2013).
19. L. A. Ponomarenko *et al.*, *Nature* **497**, 594–597 (2013).
20. R. V. Gorbachev *et al.*, *Science* **346**, 448–451 (2014).
21. Y. Cao *et al.*, *Nature* **556**, 43–50 (2018).
22. Y. Cao *et al.*, *Nature* **556**, 80–84 (2018).
23. A. L. Sharpe *et al.*, *Science* **365**, 605–608 (2019).
24. M. Serlin *et al.*, *Science* **367**, 900–903 (2020).
25. L. Li, M. Wu, *ACS Nano* **11**, 6382–6388 (2017).
26. G. Constantinescu, A. Kuc, T. Heine, *Phys. Rev. Lett.* **111**, 036104 (2013).
27. S. Zhou, J. Han, S. Dai, J. Sun, D. J. Srolovitz, *Phys. Rev. B* **92**, 155438 (2015).
28. J. H. Warner, M. H. Rümmeli, A. Bachmatiuk, B. Büchner, *ACS Nano* **4**, 1299–1304 (2010).
29. C.-J. Kim *et al.*, *Nano Lett.* **13**, 5660–5665 (2013).
30. S. M. Gilbert *et al.*, *2D Mater.* **6**, 021006 (2019).
31. H. J. Park *et al.*, *Sci. Adv.* **6**, eaay4958 (2020).
32. K. Kim *et al.*, *Nano Lett.* **16**, 1989–1995 (2016).
33. Y. Cao *et al.*, *Phys. Rev. Lett.* **117**, 116804 (2016).
34. H. Yoo *et al.*, *Nat. Mater.* **18**, 448–453 (2019).
35. A. Weston *et al.*, *Nat. Nanotechnol.* **15**, 592–597 (2020).
36. L. J. McGilly *et al.*, *Nat. Nanotechnol.* **15**, 580–584 (2020).
37. R. D. King-Smith, D. Vanderbilt, *Phys. Rev. B Condens. Matter* **47**, 1651–1654 (1993).
38. Q. Yang, M. Wu, J. Li, *J. Phys. Chem. Lett.* **9**, 7160–7164 (2018).
39. J. Sung *et al.*, *Nat. Nanotechnol.* **15**, 750–754 (2020).
40. C. R. Woods *et al.*, *Nat. Commun.* **12**, 347 (2021).
41. M. Vizner Stern *et al.*, *Science* **372**, 1462–1466 (2021).
42. See supplementary materials.
43. K. Yasuda, X. Wang, K. Watanabe, T. Taniguchi, P. Jarillo-Herrero, Replication Data for: Stacking-engineered ferroelectricity in bilayer boron nitride. Harvard Dataverse (2021); https://doi.org/10.7910/DVN/JNXOIM.

SUPPLEMENTARY MATERIALS

science.sciencemag.org/content/372/6549/1458/suppl/DC1
Materials and Methods
Figs. S1 to S26
Table S1
References (44–54)